Article

UV-Based Advanced Oxidation Processes of Remazol Brilliant Blue R Dye Catalyzed by Carbon Dots

Inês M. F. Cardoso, Rita M. F. Cardoso, Luís Pinto da Silva [ID] **and Joaquim C. G. Esteves da Silva** *[ID]

Chemistry Research Unit (CIQUP), Institute of Molecular Sciences (IMS)–DGAOT,
Faculty of Sciences of University of Porto (FCUP), Rua do Campo Alegre s/n, 4169-007 Porto, Portugal;
up201704720@edu.fc.up.pt (I.M.F.C.); up201704723@edu.fc.up.pt (R.M.F.C.); luis.silva@fc.up.pt (L.P.d.S.)
* Correspondence: jcsilva@fc.up.pt; Tel.: +351-220-402-569

Abstract: UV-based advanced oxidation processes (AOPs) (UV/H$_2$O$_2$ and UV/S$_2$O$_8$$^{2-}$) with a titanium(IV)-doped carbon dot, TiP-CD, as a catalyst were developed for the decomposition of Remazol Brilliant Blue R (Reactive Blue 19), an anthraquinone textile dye (at T = 25 °C and pH = 7). The Ti-CD, with marked catalytic UV properties, was successfully synthesized by the one-pot hydrothermal procedure, using L-cysteine as carbon precursor, ethylenediamine as nitrogen source, PEG (polyethylene glycol) as a capping agent, and titanium(IV) isopropoxide (precursor of TiO$_2$ doping). Contrary to azo dyes (methyl orange, orange II sodium salt, and reactive black 5), which achieved complete degradation in a time interval less than 30 min in the developed AOP systems (UV/H$_2$O$_2$, UV/S$_2$O$_8$$^{2-}$, and UV/TiO$_2$), the RBB-R showed relatively low degradation rates and low discoloration rate constants. In the presence of the catalyzer, the reaction rate significantly increased, and the pseudo-first-order rate constants for the RBB-R discoloration were UV/3.0 mM H$_2$O$_2$/TIP-CD-0.0330 min^{-1} and UV/1.02 mM S$_2$O$_8$$^{2-}$/TIP-CD-0.0345 min^{-1}.

Keywords: textile dyes; Remazol Brilliant Blue R; reactive blue 19; UV based AOP; nanomaterials; carbon dots
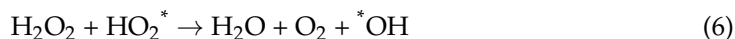
1. Introduction

The textile industry is one of the most polluting industries in the world, consuming 93 billion cubic meters of water. In fact, 20% of wastewater worldwide comes from fabric dyeing and treatment [1,2]. The increase of fast-fashion trends complicates the environmental impact of textile business, and the lack of garment eco-design inhibits efficient circular economy strategies [3]. About 80% of the global emissions of this industry are discharged into environmental water, and, although textile effluents are constituted by a huge number of chemical substances, natural fibers, and microplastics, of greater concern are the large amount of non-biodegradable organic compounds, especially textile dyes [4,5]. The treatment of these substances in wastewaters requires advanced oxidation processes (AOPs) [6]. One of the types of AOPs that can be used for the degradation of selected pollutants present in wastewater is based on ultraviolet light (UV); that is a standard technology for water disinfection, but it can also be coupled to several other chemical systems, such as, for example, hydrogen peroxide and persulfate anion, enhancing the performance in AOP [7,8].

The direct exposition of a dye (Dy) to high-energy UV light creates an excited state molecule ($^{#}$Dy) or the photolysis of a chemical bond, resulting in its fragmentation and radical formation (Dy1* + Dy2*). In the presence of molecular oxygen, reactive oxygen species can form, such as the superoxide anion (O$_2$$^{*-}$) [9]:

$$Dy + h\nu \rightarrow {}^{\#}Dy \tag{1}$$

$$^{\#}Dy \rightarrow Dy1^{*} + Dy2^{*} \tag{2}$$

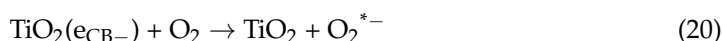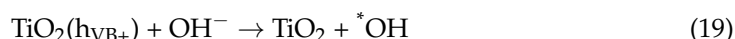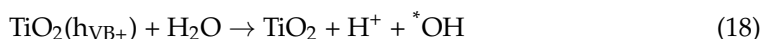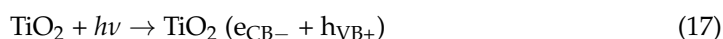$$^{\#}Dy + O_2 \rightarrow Dy^{*+} + O_2{}^{*-} \tag{3}$$

By coupling UV with hydrogen peroxide (H_2O_2), the following chain mechanism is obtained [10,11]:

$$H_2O_2 + h\nu \rightarrow 2\,{}^{*}OH \tag{4}$$

$$H_2O_2 + {}^{*}OH \rightarrow HO_2{}^{*} + H_2O \tag{5}$$

$$H_2O_2 + HO_2{}^{*} \rightarrow H_2O + O_2 + {}^{*}OH \tag{6}$$

$${}^{*}OH + {}^{*}OH \rightarrow H_2O_2 \tag{7}$$

$${}^{*}OH + HO_2{}^{*} \rightarrow H_2O + O_2 \tag{8}$$

$$HO_2{}^{*} + HO_2{}^{*} \rightarrow H_2O_2 + O_2 \tag{9}$$

By coupling UV with persulfate anion ($S_2O_8{}^{2-}$), the following chain mechanism is obtained [11–13]:

$$S_2O_8{}^{2-} + h\nu \rightarrow 2\,SO_4{}^{*-} \tag{10}$$

$$H_2O + SO_4{}^{*-} \rightarrow HSO_4{}^{-} + {}^{*}OH \tag{11}$$

$$S_2O_8{}^{2-} + SO_4{}^{*-} \rightarrow S_2O_8{}^{*-} + SO_4{}^{2-} \tag{12}$$

$${}^{*}OH + S_2O_8{}^{2-} \rightarrow S_2O_8{}^{*-} + OH^{-} \tag{13}$$

$${}^{*}OH + {}^{*}OH \rightarrow H_2O_2 \tag{14}$$

$$SO_4{}^{*-} + {}^{*}OH \rightarrow HSO_5{}^{-} \tag{15}$$

$$SO_4{}^{*-} + SO_4{}^{*-} \rightarrow S_2O_8{}^{2-} \tag{16}$$

Coupling UV with H_2O_2 and $S_2O_8{}^{2-}$ will generate the hydroxyl radical and, in the case of $S_2O_8{}^{2-}$, the sulfate radical, and these radical species are active oxidants in the dyes' degradation processes [11]. Besides these two homogeneous catalysts, the heterogeneous photocatalyst and semiconductor TiO_2 is also commonly used as an AOP, and hydroxyl radical is produced according to the following mechanism [14–18]:

$$TiO_2 + h\nu \rightarrow TiO_2\,(e_{CB-} + h_{VB+}) \tag{17}$$

$$TiO_2(h_{VB+}) + H_2O \rightarrow TiO_2 + H^{+} + {}^{*}OH \tag{18}$$

$$TiO_2(h_{VB+}) + OH^{-} \rightarrow TiO_2 + {}^{*}OH \tag{19}$$

$$TiO_2(e_{CB-}) + O_2 \rightarrow TiO_2 + O_2{}^{*-} \tag{20}$$

After TiO_2 UV absorption, an electron (e_{CB-}) in the valence band is transferred to the conduction band, leaving a hole in the valence band (h_{VB+}). The $TiO_2(h_{VB+})$ will oxidize water, and $TiO_2(e_{CB-})$ will reduce oxygen-generating reactive oxygen species such as hydroxide and superoxide radicals.

Nanomaterials are being coupled with UV-based AOP to make treatment processes more sustainable, i.e., to eliminate or reduce the amount of chemical substances involved in those processes, while increasing the pollutants degradation yields [6]. Taking into consideration natural resources, environmental sustainability, and toxicity issues, carbon-based nanomaterials are being preferred to metallic/semi-metallic materials in real-world applications [19]. Among the carbon-based nanomaterials, the synthetic versatility of carbon dots (CDs) [20–29] makes them the preferable choice to be coupling to an AOP for the treatment of textile wastewater.

Carbon dots are synthesized to achieve a desirable reactivity. In this paper, we describe the synthesis of a CD to be a catalyzer of the dye decomposition upon UV coupled with H_2O_2 and $S_2O_8{}^{2-}$ AOPs. Because we were developing catalytic-based AOP, the objective was to increase the concentration of the hydroxyl radical and improve the dye decomposi-

tion or wastewater discoloration. In this work, the rational for the synthesis design had the following criteria:

1. To promote the decomposition of an oxidant molecule such as H_2O_2 and $S_2O_8^{2-}$, an antioxidant is necessary. We have been using L-cysteine as a carbon precursor in CD synthesis [5]. Moreover, due to the existence of SH functional groups, it has antioxidant properties [30];

2. To increase the surface reactivity of the CD, the doping with a semiconductor such as TiO_2, which is excited when exposed to UV light, was used. Indeed, this strategy has already been used for the production of photocatalytic carbon-based nanoparticles [31–33].

3. Polyethylene glycol (PEG) has been used in CD synthesis to increase the water solubility and to coat the CD with a soft surface [5]. Indeed, PEG undergoes caramelization, leading to the production of PEGylated nanoparticles [7,34–37].

In this paper, we describe the synthesis of two titanium(IV)-doped carbon-based nanomaterials (carbon dot), one with PEG (TiP-CD) and another without PEG (Ti-CD), that were used as catalysts in the UV based AOP discoloration of the anthraquinone dye, the Remazol Brilliant Blue R (also known as Reactive Blue 19) (RBB-R). Moreover, the performance of UV-based AOP (UV, UV/H_2O_2, UV/$S_2O_8^{2-}$, and UV/TiO_2) was assessed in the discoloration of aqueous solutions of azo dyes, methyl orange (MO), orange II sodium salt (O-II), and reactive black 5 (RB-5), besides RBB-R.

2. Materials and Methods

2.1. Reagents

Polyethylene glycol with an average molecular weight of 200 (PEG) (Sigma-Aldrich, St. Louis, MO, USA, P3015), L-cysteine (Sigma-Aldrich, St. Louis, MO, USA, W326305), titanium(IV) isopropoxide (Aldrich, St. Louis, MO, USA, 87560), ethylenediamine (Aldrich, St. Louis, MO, USA, E2,626-6), titanium dioxide (Sigma-Aldrich, St. Louis, MO, USA, anatase nanopowder <25 nm, 637254), hydrogen peroxide (Chem-Lab, Zedelgem, Belgium, CL00.2308), and sodium persulfate (Sigma-Aldrich, St. Louis, MO, USA, 216232) were used. The dyes used in this work were similar to those described in reference [5]. The chemical structure of the anthraquinone dye RBB-R is shown in Figure 1.
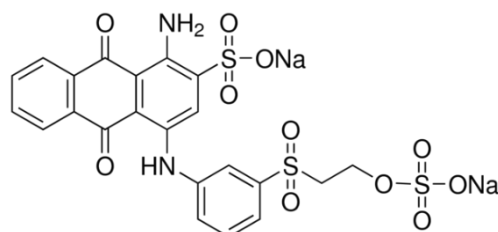

Figure 1. Chemical structure of Remazol Brilliant Blue R (Reactive Blue 19) (RBB-R).

2.2. Synthesis of Titanium(IV)-Doped Carbon Dots (Ti-CD)

A one-pot button-up hydrothermal process was used for the Tip-CD and Ti-CD synthesis. The following solution was prepared for hydrothermal treatment: 0.400 g of L-cysteine was dissolved in 30 mL of water; after, only for the Tip-CD sample, 6.00 mL of PEG was used, and 0.60 mL of ethylenediamine was added and homogenized; lastly, 1.00 mL of titanium(IV) isopropoxide was added to the previous solution. The resulting mixture was placed in a Parr Series 4700 Pressure Vessel and treated hydrothermally for 5 h at 200 °C. The purification procedure was similar to that described in Reference [5].

2.3. UV Advanced Oxidation Process (AOP)

A 254 nm UV lamp system for water disinfection (25 W low-pressure mercury lamp S463RL, UV model S5Q-PA/2, VIQUA, Guelph, ON, Canada) was used. Experiments were carried out at pH = 3.00, 7.00, and 10.00, using the same methodology as described in

Reference [5]. At the end of the experiments, the pH of the treated solutions was measured, and at pH = 3 experiments, it remained constant, but, at the pH = 7 and 10 experiments, it decreased to about 1 pH unit.

The initial concentration of the dye aqueous solutions was similar to that described in Reference [5]. For the analysis of the effect of the Tip-CD and Ti-CD, 0.500 mL of the solution was used.

2.4. Equipment

The synthesized carbon dots were characterized by using the following the equipment. Fluorescence analysis was measured in a 10 mm fluorescence quartz cell by using a Horiba Jobin Yvon FluoroMax spectrofluorimeter (New Jersey, NJ, USA), using 5 nm slit widths. The Zeta Potential was measured by using a particle analyzer Anton Paar Litesizer^{TM} 500 (Graz, Austria) and a polycarbonate Omega Cuvette (Ref. 155765). Fourier-transform infrared (FTIR) spectra were measured with a Perkin-Elmer (Waltham, MA, USA) Spectrum Two with an ATR sampling accessory. UV–Vis spectra were acquired with a VWR UV3100-PC spectrophotometer (Avantor, Radnor, PA, USA). AFM analysis was carried out by using a Veeco (Plainview, NY, USA) Metrology Multimode/Nanoscope IVA by tapping mode, using a Bruker (Billerica, MD, USA) silicon probe (model TESP-SS, resonant frequency of 320 kHz, nominal force constant of 42 N/m, and estimated tip radius of 2 nm). Scanning electron microscopy, SEM, was performed with a Quanta 200 from FEI Company (Hillsboro, OR, USA) coupled with energy dispersive spectroscopy (SEM–EDS).

2.5. Data Analysis

The registry of the absorbance of the dyes' aqueous solutions as a function of the time of exposition to the UV light was carried out at the maximum absorbance of the dyes [5]. The percentage of dye removal (%DR), the apparent pseudo-first-order rate constant (k_{ap} without catalyst, k_{ap}^c with H_2O_2, $Na_2S_2O_8$, or TiO_2 catalyst and k_{ap}^N with nanomaterial), the percentage of increase of the rate constant when the catalyst is present (%Inc) and the percentage of increase of the rate constant when the nanomaterial is present (%Inc^N) were calculated by using Equations (21)–(24), respectively (a linear relation between the absorbance and the aqueous concentration of the dyes was observed):

$$\%DR = 100 \times (Abs_0 - Abs_t)/Abs_0 \tag{21}$$

$$\ln(Abs_t/Abs_0) = -k_{ap}\, t \tag{22}$$

$$\%Inc = 100 \times (k_{ap}^c - k_{ap})/k_{ap} \tag{23}$$

$$\%Inc^N = 100 \times (k_{ap}^N - k_{ap}^c)/k_{ap}^c \tag{24}$$

where Abs_0 and Abs_t are the absorbances of the dye aqueous solution at initial and t time of UV exposition.

3. Results

3.1. UV AOP of Dyes

The UV exposition of the aqueous solutions of the dyes resulted differently for the four dyes and pH values under analysis (Figure 2 shows an example of the pH = 10 experiments). The analysis of the spectra as function of the time of UV exposition shows that the visible part of the spectra decreases the absorbance (discoloration), but, in the UV section of the spectra, absorption bands show different trends, suggesting the formation followed by degradation of other intermediate molecular fragments. Table 1 presents the discoloration kinetics parameters resulting from the UV AOP of the aqueous solutions of the dyes at three pH values: 3, 7, and 10.
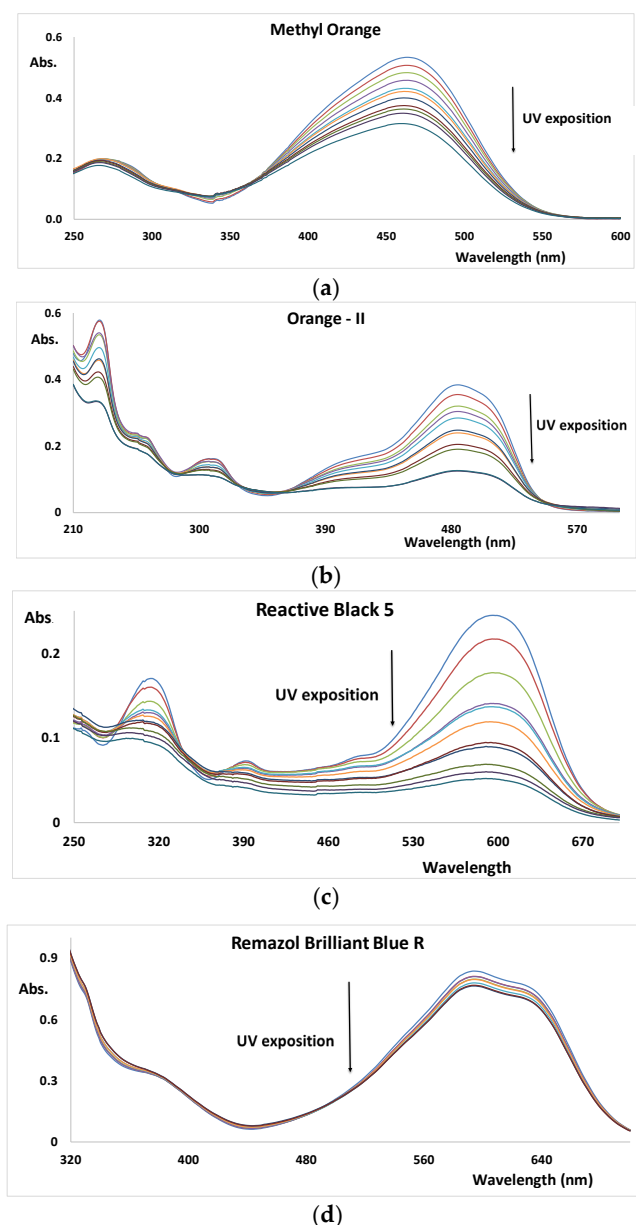
Figure 2. UV–Vis spectra of dyes as function of the UV exposition (pH = 10, and reaction time = 30 min). (**a**) Methyl orange; (**b**) Orange-II; (**c**) Reactive Black 5; and (**d**) Remazol Brilliant Blue R.

The analysis of Table 1 shows that the discoloration apparent rate constants of the azo dyes are about ten times bigger than those of RBB-R. Moreover, for the two azo dyes, O-II and RB-5, the discoloration rate is bigger at pH = 10, with a rate constant value of about 0.04 min^{-1} and with a percentage of dye removal of about 70% in 30 min. The third azo dye show a lower decomposition time and has the biggest rate constant at pH = 3, at about 0.03 min^{-1}, with a %DR of about 60% in 30 min. The anthraquinone dye RBB-R has a relatively lower rate constant, as can clearly be observed in Figure 2, achieving a maximum %DR of about 20% (30 min) at pH = 3.

In order to try to improve the decomposition rates of the dyes, UV was coupled with H_2O_2, $S_2O_8^{2-}$, and TiO_2. Because the pH of wastewaters of textile is close to neutral [5], the following work focused on aqueous solutions at pH = 7.

Table 1. Apparent rate constant and percentage of dye removal (at 30 min) of the UV AOP of dyes (the standard deviations of at least three independent repetitions are shown). The fitting of the integrated first-order kinetics resulted in $R^2 > 0.98$.

Dye	pH	k_{ap} (min^{-1})	%DR
	3	0.0294 ± 0.0108	63.53 ± 3.56
MO	7	0.0051 ± 0.0006	15.23 ± 1.94
	10	0.0169 ± 0.0012	40.58 ± 0.27
	3	0.0129 ± 0.0003	33.73 ± 0.83
O-II	7	0.0133 ± 0.0016	32.53 ± 3.16
	10	0.0337 ± 0.0006	64.50 ± 2.57
	3	0.0227 ± 0.0006	47.37 ± 3.42
RB-5	7	0.0235 ± 0.0007	48.39 ± 1.94
	10	0.0474 ± 0.0046	78.07 ± 1.03
	3	0.0078 ± 0.0009	22.20 ± 3.10
RBB-R	7	0.0034 ± 0.0003	9.16 ± 0.32
	10	0.0025 ± 0.0009	7.78 ± 2.82

3.2. UV/H$_2$O$_2$ AOP of Dyes

Table 2 and Figure 3 show the results obtained for the four dyes under the UV + H$_2$O$_2$ AOP. Coupling UV with a relatively low concentration of hydrogen peroxide of 0.3 mM allowed the AOP to reach almost complete discoloration of the azo dyes, but within different exposition times: MO, 30 min; O-II, 10 min; and RB-5, 4 min. However, at this H$_2$O$_2$ concentration, the decomposition of the RBB-R achieved only about 14% in 30 min. For the decomposition of RBB-R to reach about 96%, it was necessary to use a 100-times-higher H$_2$O$_2$ concentration.

The discoloration-rate values of the dyes studied in this work are higher than most results reported in the literature for the same dyes when UV/H$_2$O$_2$ AOP was used. One study evaluated the effectiveness of RB-5 bleaching through the UV/H$_2$O$_2$ system, in which a k_{ap} value of 0.105 min^{-1} was obtained (pH = 7) [38]. The degradation of MO was studied by using a UV/H$_2$O$_2$ process, and the almost complete degradation of MO was achieved in just 3 min when 0.1 mL of H$_2$O$_2$ was added to 20 mL of MO solution [39]. Four Fe-containing materials were used as heterogeneous photochemical catalysts for the discoloration of O-II in the presence of H$_2$O$_2$ and UV-C (pH values of 3 and 6), and the k_{ap} increased from 0.050 to 0.193 min^{-1} [40]. The discoloration of RB-5 was investigated through the UV/H$_2$O$_2$ process, which resulted in k_{ap} values ranging from 0.01 to 0.042 min^{-1} [41]. The discoloration capacity of RB-5 was evaluated through the advanced photochemical process ferrioxalate/H$_2$O$_2$/UV-C, in which a k_{ap} value of 0.0922 min^{-1} was obtained [42].

Table 2. Apparent first-order rate constant, percentage of the rate constant when the catalyst is present, and percentage of dye discoloration of the UV + H$_2$O$_2$ AOP of dyes (the standard deviations of at least three independent repetitions are shown). In parentheses, the reaction time necessary to achieve the percentage of dye removal is shown. The fitting of the integrated first-order kinetics resulted in $R^2 > 0.98$.

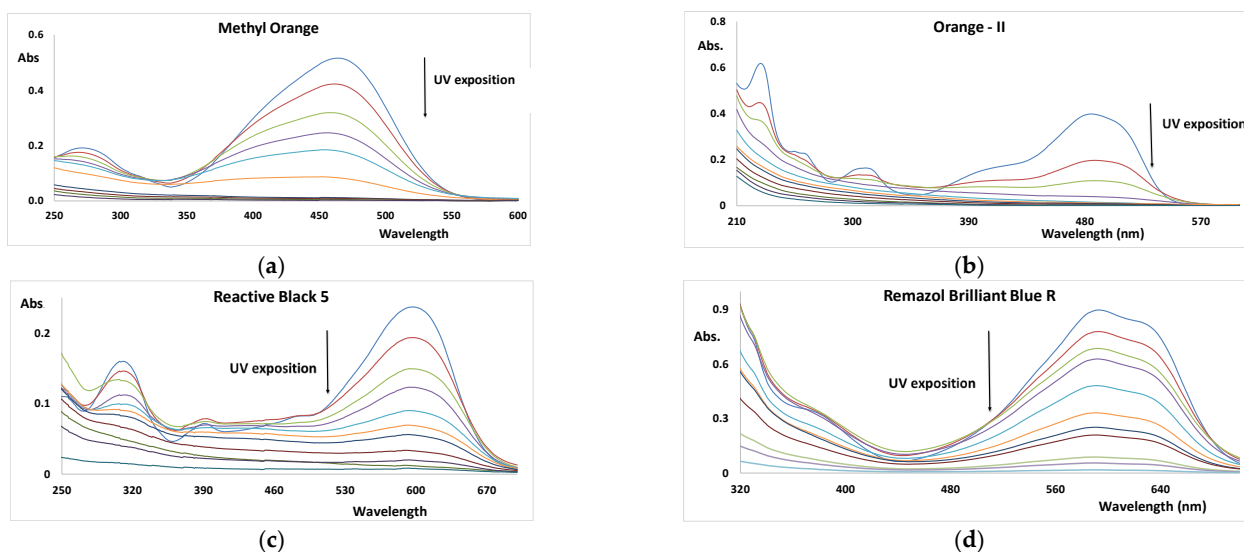| Dye	$k_{ap}{}^c$ (min^{-1})	%Inc	%DR
MO + 0.30 mM H$_2$O$_2$	0.2294 ± 0.0179	4398	99.95 ± 0.03 (30 min)
O-II + 0.30 mM H$_2$O$_2$	0.5921 ± 0.1465	4352	98.64 ± 0.46 (10 min)
RB-5 + 0.30 mM H$_2$O$_2$	0.9017 ± 0.0773	3737	96.19 ± 1.93 (4 min)
RBB-R + 0.30 mM H$_2$O$_2$	0.0046 ± 0.0007	35	13.87 ± 1.84 (30 min)
RBB-R + 3.0 mM H$_2$O$_2$	0.0091 ± 0.0016	168	23.72 ± 1.76 (30 min)
RBB-R + 30 mM H$_2$O$_2$	0.1169 ± 0.0121	3338	96.22 ± 1.43 (30 min)

Figure 3. UV–Vis spectra of dyes as function of the UV/H_2O_2 exposition (pH = 7, and reaction time = 30 min). (**a**) Methyl orange; (**b**) Orange-II; (**c**) Reactive Black 5; and (**d**) Remazol Brilliant Blue R.

3.3. $UV/S_2O_8{}^{2-}$ AOP of Dyes

Table 3 shows the results obtained for the four dyes under the UV + Persulfate AOP. Coupling UV with a concentration of persulfate higher than 0.1 mM allowed the AOP of the azo dyes to reach a discoloration percentage higher than 90% (at 30 min). However, for the decomposition of RBB-R to reach about 90%, an 80-times-higher persulfate concentration is necessary. This result shows that a similar relatively low efficiency, when compared with the azo dyes, for the RBB-R degradation is achieved with the UV/persulfate AOP when compared with the UV/H_2O_2 AOP.

Table 3. Apparent first-order rate constant, percentage of the rate constant when the catalyst is present, and percentage of dye discoloration of the $UV + S_2O_8{}^{2-}$ AOP of dyes (the standard deviations of at least three independent repetitions are shown). In parentheses, the reaction time necessary to achieve the percentage of dye removal is shown. The fitting of the integrated first-order kinetics resulted in $R^2 > 0.98$.

Dye	$k_{ap}{}^c$ (min^{-1})	%Inc	%DR
MO + 0.10 mM Na$_2$S$_2$O$_8$	0.0677 ± 0.0010	1227	87.05 ± 0.78 (30 min)
MO + 1.02 mM Na$_2$S$_2$O$_8$	0.9365 ± 0.0810	18,263	98.56 ± 0.60 (5 min)
O-II + 0.010 mM Na$_2$S$_2$O$_8$	0.0255 ± 0.0205	400	54.08 ± 0.42 (30 min)
O-II + 0.10 mM Na$_2$S$_2$O$_8$	0.4498 ± 0.0280	8720	94.99 ± 3.39 (30 min)
O-II + 1.02 mM Na$_2$S$_2$O$_8$	1.1187 ± 0.1949	21,835	98.86 ± 0.31 (5 min)
RB-5 + 0.010 mM Na$_2$S$_2$O$_8$	0.0601 ± 0.0042	1078	80.74 ± 4.24 (30 min)
RB-5 + 0.10 mM Na$_2$S$_2$O$_8$	0.5608 ± 0.0606	10,896	91.03 ± 4.68 (5 min)
RBB-R + 0.010 mM Na$_2$S$_2$O$_8$	0.0017 ± 0.0049	-50	5.31 ± 1.21 (30 min)
RBB-R + 1.02 mM Na$_2$S$_2$O$_8$	0.0277 ± 0.0049	715	58.70 ± 7.36 (30 min)
RBB-R + 2.04 mM Na$_2$S$_2$O$_8$	0.0531 ± 0.0108	1462	80.39 ± 5.93 (30 min)
RBB-R + 4.07 mM Na$_2$S$_2$O$_8$	0.0712 ± 0.0024	1994	81.59 ± 4.87 (30 min)
RBB-R + 8.15 mM Na$_2$S$_2$O$_8$	0.0960 ± 0.0056	2724	95.25 ± 1.21 (30 min)

The discoloration-rate values of the dyes, as shown in Table 3, are higher than most results reported in the literature for the same dyes when using AOPs based on the sulfate radical: namely, a UV/persulfate process was used for the degradation of MO, with a k_{ap} of 0.7 min^{-1} (25 °C) after 15 min [43]; the degradation of O-II by the AOP based on sulfate radical mediated by Fe^o@Fe$_x$O$_y$ particles was investigated, and a k_{ap} of 0.057 min^{-1} was obtained [44]; Fe$_3$O$_4$ magnetic nanoparticles were used to activate

peroxymonosulfate (PMS) in the degradation of RB-5, and when the PMS dosage increased from 0.25 to 2 mM, the kinetic rate constant showed the same trend, with an increase of 0.0085 min^{-1} to 0.0387 min^{-1} [45]; for the degradation of O-II, copper phosphide (Cu_3P) was used as a heterogeneous catalyst for the activation of peroxydisulfate (PDS), and the k_{ap} was 0.1306 min^{-1} (pH = 7) [46]; and a persulfate system, activated by a nanocompound (α-FeOOH@GCA + $K_2S_2O_8$), was applied for the discoloration of O-II, and a k_{ap} of 0.0502 min^{-1} was obtained [47].

3.4. UV/TiO_2 AOP of Dyes

Table 4 shows the results obtained for the four dyes under the UV + TiO_2 AOP, using a concentration of 0.050 g of TiO_2/L. Comparing these results with the simple UV AOP, we see that large increases (between 151 and 331) in the discoloration are observed for the azo dyes. On the contrary, the presence of TiO_2 almost does not affect the discoloration of RBB-R.

Table 4. Apparent rate constant, percentage of the rate constant when the catalyst is present, and percentage of dye removal of the UV + TiO_2 AOP of dyes (the standard deviations of at least three independent repetitions are shown). In parentheses, the reaction time necessary to achieve the percentage of dye removal is shown. The fitting of the integrated first-order kinetics resulted in $R^2 > 0.98$.

Dye	$k_{ap}{}^c$ (min^{-1})	%Inc	%DR
MO + 0.050 g/L TiO$_2$	0.0220 ± 0.0032	331	48.92 ± 5.28 (30 min)
O-II + 0.050 g/L TiO$_2$	0.0409 ± 0.0022	208	68.69 ± 1.96 (30 min)
RB-5 + 0.050 g/L TiO$_2$	0.0591 ± 0.0085	151	66.12 ± 2.22 (30 min)
RBB-R + 0.050 g/L TiO$_2$	0.0035 ± 0.0009	3	8.87 ± 1.29 (30 min)

As shown in Table 4, the presence of TiO_2 increased the rate of discoloration of the dyes. The catalytic effect of the UV/TiO_2 AOP is well-known, and, for the dyes under investigation, the following results from the literature can be found: the effectiveness of RB-5 bleaching through the UV/TiO_2 system had a k_{ap} value of 0.033 min^{-1} (pH = 7) [38]; TiO_2 nanoparticles (NPs) were used in the degradation of MO under UV radiation, and the k_{ap} ranged from 0.005 to 0.0063 min^{-1} [48]; one study demonstrated efficient degradation of the O-II and RB-5 dyes through the UV/TiO_2 photocatalytic system, with a k_{ap} of 0.025 and 0.005 min^{-1}, respectively [49]; the photocatalytic discoloration of RB-5 in the presence of TiO_2 nanoparticles under UV radiation was studied, and the k_{ap} values ranged from 0.01 to 0.125 min^{-1} [50]; a photocatalytic reactor with an ozone-generating mercury vapor lamp and TiO_2 was used for the degradation of MO, and the k_{ap} was 0.0473 min^{-1} [51]; and the photocatalytic degradation of RBB-R was studied with thin films of nitrogen-doped TiO_2 catalysts under UV-A radiation, and the values were $k_{ap} = 5.1 \times 10^{-5}$ (undoped), $k_{ap} = 1.8 \times 10^{-4}$ (doped with 0.72% of N), and $k_{ap} = 2.0 \times 10^{-4}$ (doped with 0.84% of N) [52].

The above UV-based AOPs are not very effective for the anthraquinone dye RBB-R decomposition unless relatively high concentrations of hydrogen peroxide and persulfate are used; however, this raises sustainability problems. As an alternative, a carbon-based nanocatalyst was developed to be coupled to UV and hydrogen peroxide or persulfate to increase the efficiency of the RBB-R discoloration.

3.5. Preliminary Analysis of the Catalytic Performance of the Synthesized CD

The basic precursors of the CD developed in this project were L-cysteine and ethylenediamine, which were used as carbon and nitrogen sources, respectively. The other two components, PEG and the titanium compound, were analyzed for their essential role in the final photocatalyst. Taking into consideration the critical role of PEG previously observed in the ozonation catalyst [5], two CDs were synthesized with (TiP-CD) and without PEG (Ti-CD). The preliminary comparative analysis of the two photocatalysts confirmed that PEG is essential to the observed photocatalysis, and this observation is further supported

below. In the case of titanium doping (namely TiO$_2$), a CD was synthesized by using the composition described for TiP-CD (Section 2.2), but without the titanium compound. The catalytic discoloration properties of this non-doped CD was markedly worse than the TiP-CD. For this reason, the work focused mainly on TiP-CD investigation.

3.6. Characterization of the Nanomaterials

In aqueous solution, the nanomaterials become agglomerated and hydrated, as seen the DLS results shown in Figure 4a, with an average hydrodynamic size of about 310 and 297 nm for Ti-CD and TiP-CD, respectively. Figure 4b shows that the mean Zeta potential is −0.3 and −3.5 mV for Ti-CD and TiP-CD, respectively, with a charge distribution ranging from slightly positively charged to slightly negatively charged nanoparticles. Figure 5 shows the AFM images of the TiP-CD. The analysis of the AFM results shows that they have a spherical shape, with an average size of 22 ± 3 nm.
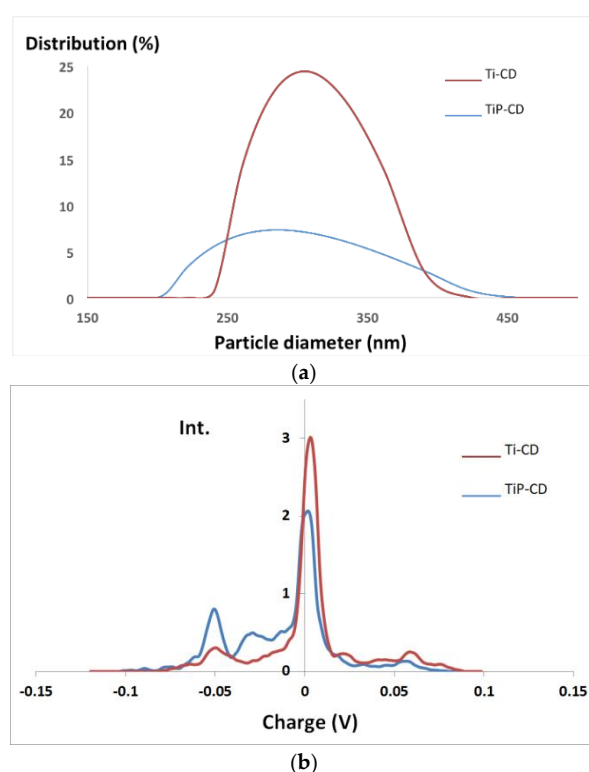

(**a**)

(**b**)

Figure 4. (**a**) DLS spectra and (**b**) Zeta potential of Ti-CD and TiP-CD.
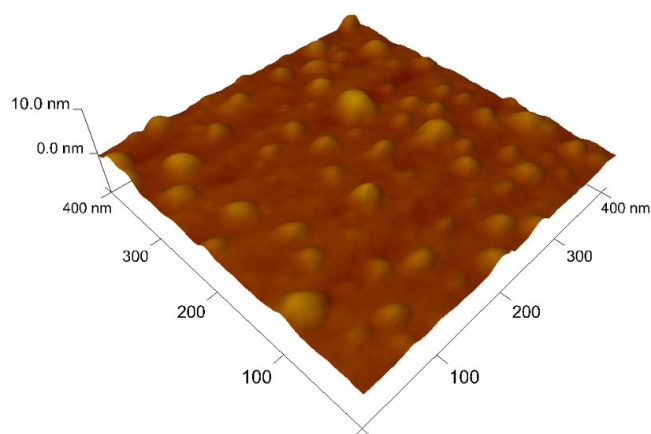

Figure 5. AFM image of TiP-CD.

Figure 6 shows the SEM and EDS of Ti-CD (Figure 6a,d) and TiP-CD (Figure 6b,c,e) samples. The morphology of the two samples, as revealed by SEM, is rather different. While Ti-CDs (Figure 6a) have a nanotube shape, with a diameter of about 35 nm, and are highly agglomerated into bigger clusters, the TiP-CDs (Figure 6b,c) are dispersed with a PEG capping (particularly clear in Figure 6b) that confirm the size determined by AFM; Figure 6c shows as an example a nanoparticle with a size of 21 nm. This result shows the role of PEG on the capping, dispersion, and shape of the nanoparticles. The EDS of the two samples confirm the titanium doping, particularly in the Ti-CD sample (Figure 6d). In the case of TiP-CDs, because they are highly dispersed and capped with PEG, titanium is hardly detected, but, as expected, the presence of carbon, oxygen, and sulfur is clearly observed.
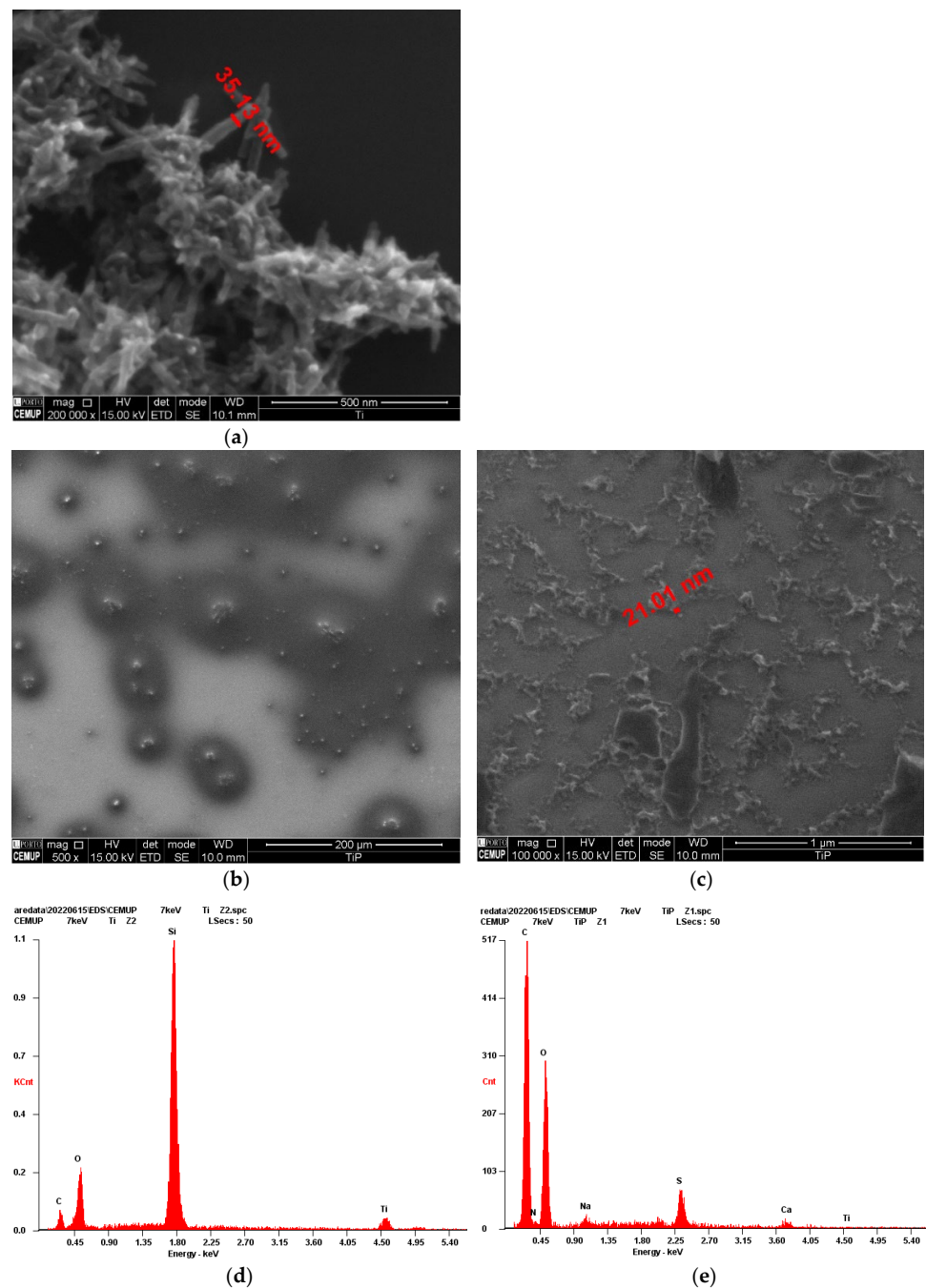

Figure 6. SEM images of the Ti-CD (**a**) and TiP-CD (**b**,**c**) samples and the corresponding EDS (Ti-CD (**d**) and TiP-CD (**e**)).

Figure 7 shows the UV–Vis (Figure 7a), FTIR (Figure 7b), and fluorescence emission at the maximum of the excitation (325 nm) (Figure 7c) spectra of both the CD and the lifetime decay of TiP-CD (Figure 7d). The UV–Vis spectra of both samples (Figure 5a) are characterized by a main band at 317 nm and a shoulder at 286 nm. These spectra are similar to other CDs' spectra, with a strong absorption in the ultraviolet that tails into the visible region due to the n–χ^* transition of multi-conjugate C=O [53,54].
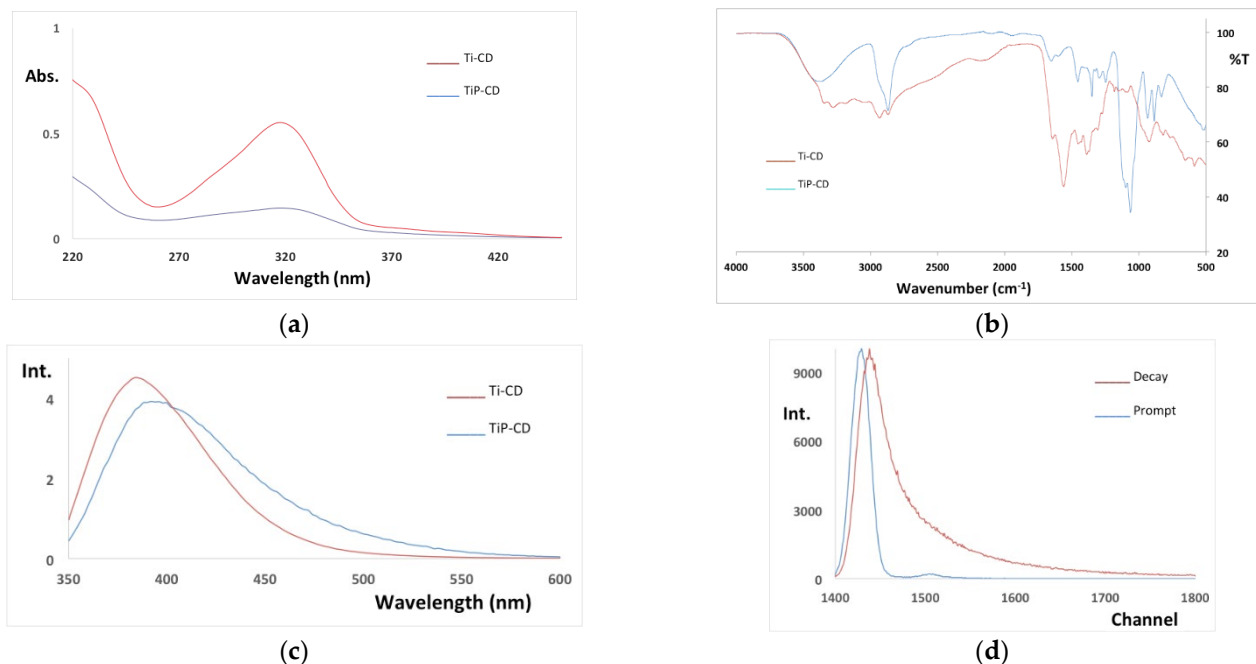

Figure 7. (**a**) UV–Vis, (**b**) FTIR, (**c**) fluorescence emission (ex. 350 nm) spectra of Ti-CD and TiP-CD, and (**d**) fluorescence lifetime decay.

The FTIR spectra of Ti-CD and TiP-CD (Figure 7b) are rather different due to the PEG capping of sample TiP-CD. The spectrum of Ti-CD is characterized by the following main bands [53–55]: C=O stretching can be observed at 1652 cm^{-1}; C–C stretching bands are located at 1568 and 1461 cm^{-1}; the bands at 3205, 3300, and 3362 cm^{-1} are related to the stretching vibration of N–H and O–H bonds; the bands at 1397 and 1386 cm^{-1} are attributed to the bending modes of O–H and/or C–H; and the stretching vibration of C–H bonds appeared at 2947 and 2884 cm^{-1}. The FTIR spectrum of TiP-CD is dominated by the bands due to PEG [56,57]: C–O and C–C stretching and CH$_2$ rocking at 841 cm^{-1}; CH$_2$ rocking and CH$_2$ twisting at 939 cm^{-1}; C–O and C-C stretching and CH$_2$ rocking at 1066 cm^{-1}; C–O and C–C stretching at 1105 cm^{-1}; C–O stretching and CH$_2$ rocking at 1105 cm^{-1}; CH$_2$ twisting at 1226 cm^{-1}; CH$_2$ wagging at 1353 cm^{-1}; CH$_2$ scissoring at 1461 cm^{-1}; C-H stretching at 2896 cm^{-1}; and O-H stretching at 3418 cm^{-1}.

The fluorescence emission spectra characterized by a broad band with a maximum at 384 and 394 nm for Ti-CD and TiP-CD, respectively, that are responsible for a typical blue emission of CD [58–60]. The lifetime decay of the TiP-CD fits (with a χ^2 = 1.25) a three-fluorophores model with the following lifetimes (pre-exponential factors under parenthesis): 0.69 $\pm$ 0.02 ns (0.0508 $\pm$ 0.0003), 2.67 $\pm$ 0.08 ns (0.0241 $\pm$ 0.0001), and 2.67 $\pm$ 0.08 ns (0.00583 $\pm$ 0.00003).

3.7. UV-Based AOP of RBB-R in the Presence of TiP-CD

The effect of the addition of the TiP-CD in the UV/H$_2$O$_2$ and UV/persulfate degradation kinetics of the RBB-R dye is shown in Figure 8 and Table 5. The presence of Ti-CD or TiP-CD on the single UV AOP of RBB-R inhibits the discoloration rate. However, in the UV/H$_2$O$_2$ and UV/persulfate AOP, a marked increase in the discoloration rate is observed

when TiP-CD is present, reaching a 263% increase. However, as expected from the initial catalytic evaluation of both nanomaterials, the effect of Ti-CD is null. This result supports the important role of the PEG capping in the nanocatalysts of AOP [5].
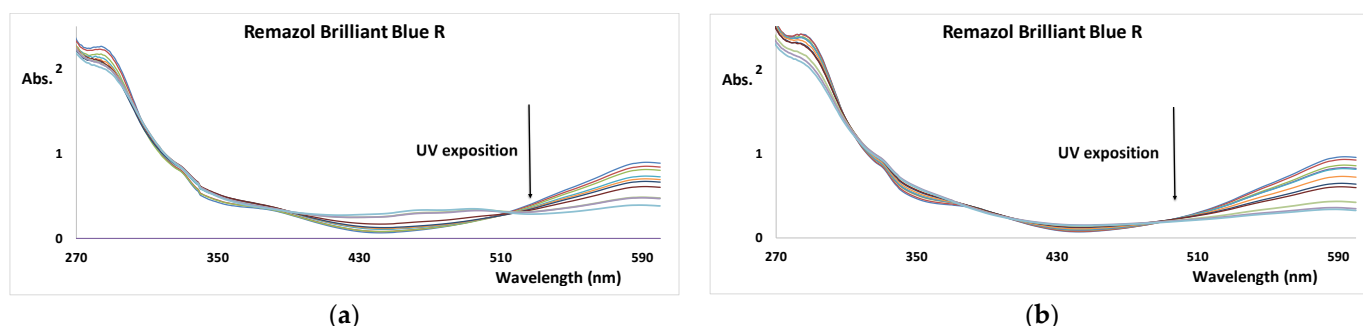

(a)

(b)

Figure 8. UV–Vis spectra of RBB-R as function of the **(a)** $UV/H_2O_2/TiP$-CD and **(b)** $UV/S_2O_8^{2-}/TiP$-CD exposition (pH = 7, and reaction time = 30 min).

Table 5. Apparent rate constant, percentage of the rate constant when Ti-CD is present, and percentage of dye removal (at 30 min) of the UV + Ti-CD AOP of RBB-R (the standard deviations of at least three independent repetitions are shown). The fitting of the integrated first-order kinetics resulted in $R^2 > 0.98$.

	k_{ap}^N **(min^{-1})**	**%Inc^N**	**%DR**
RBB-R + TiP-CD	0.0029 ± 0.0003	-14	8.02 ± 0.88
RBB-R + Ti-CD	0.0023 ± 0.0003	-32	7.17 ± 0.71
RBB-R + 0.30 mM H_2O_2 + TiP-CD	0.0071 ± 0.0021	54	17.83 ± 5.29
RBB-R + 3.0 mM H_2O_2 + TiP-CD	0.0330 ± 0.0087	263	57.91 ± 8.91
RBB-R + 3.0 mM H_2O_2 + Ti-CD	0.0079 ± 0.0013	1.3	21.12 ± 3.51
RBB-R + 0.010 mM $Na_2S_2O_8$ + TiP-CD	0.0021 ± 0.0001	24	6.18 ± 0.40
RBB-R + 1.02 mM $Na_2S_2O_8$ + TiP-CD	0.0345 ± 0.0032	25	63.35 ± 1.99
RBB-R + 1.02 mM $Na_2S_2O_8$ + Ti-CD	0.0236 ± 0.0014	6	52.59 ± 0.65

Taking into consideration that the decomposition of the dyes occurs due to the reaction with the hydroxyl (mainly Equations (4), (6), (11), and (18)) and sulfate (Equation (10)) radicals, the presence of TiP-CD will somehow promote the formation of these highly oxidant species. The enhancement of photodegradation of RBB-R in the presence of TiP-CD and H_2O_2 or $S_2O_8^{2-}$ may be attributed to the combined effects of photodissociation of the oxidant species in the presence of UV light and TiP-CD surface, the presence of the hydroxyl radical species on the reactant mixture, and the PEG coating together with the dye [61]. A hypothesis of the direct role of TiP-CD may be in the surface catalyzed hydroxyl radical formation, as described in Equation (25) for the case of H_2O_2 [62]:

$$TiP\text{-}CD + H_2O_2 \rightarrow TiP\text{-}CD^+ + OH^- + {}^*OH \tag{25}$$

4. Conclusions

A titanium(IV)-doped and PEG-capped carbon dot synthesized from L-cysteine and ethylenediamine (TiP-CD) showed itself to be an efficient catalyst for the UV/H_2O_2 and UV/persulfate AOP. Indeed, marked increases of up to 263% of the discoloration rate of the anthraquinone dye RBB-R were observed when the TiP-CD was present; this can open up new sustainable AOP strategies for the degradation of families of dyes that are difficult to degrade. Discoloration pseudo-first-order rate constants in the order of 0.034 min^{-1} were obtained with both UV/H_2O_2 and UV/persulfate AOP systems.

AOP, UV/H_2O_2, and UV/persulfate generate the hydroxyl radical upon UV exposition, and, in the case of persulfate, the radical sulfate, the observed catalytic role of the carbon-based nanomaterial is related to an increase of the hydroxyl radical production.

Moreover, because PEG is crucial for the observed catalytic effect, and PEG is capping the nanoparticle, the active substrate, H_2O_2, and persulfate anion will become trapped in the gelified external layer of the nanoparticle, and the UV-activated core will decompose the substrate into hydroxyl and sulfate radicals.

References

1. The World Bank. How Much Do Our Wardrobes Cost to the Environment? 2019. Available online: https://www.worldbank.org/en/news/feature/2019/09/23/costo-moda-medio-ambiente (accessed on 18 April 2022).
2. European Parliament News. The Impact of Textile Production and Waste on the Environment (Infographic). 2020. Available online: https://www.europarl.europa.eu/news/en/headlines/society/20201208STO93327/the-impact-of-textile-production-and-waste-on-the-environment-infographic (accessed on 18 April 2022).
3. ECOS. Ecodesign Requirements for Textiles are a Crucial Step Towards Stopping Fast Fashion. 2021. Available online: https://ecostandard.org/news_events/ecos-report-durable-repairable-and-mainstream/ (accessed on 18 April 2022).
4. Lellis, B.; Fávaro-Polonio, C.Z.; Pamphile, J.A.; Polonio, J.C. Effects of textile dyes on health and the environment and bioremediation potential of living organisms. *Biotechnol. Res. Innov.* **2019**, *3*, 275–290. [CrossRef]
5. Cardoso, I.M.F.; Cardoso, R.M.F.; da Silva, L.P.; Esteves da Silva, J.C.G. Copper(II) doped carbon dots as catalyzer of ozone degradation of textile dyes. *Nanomaterials* **2022**, *12*, 1211. [CrossRef] [PubMed]
6. Cardoso, I.M.F.; Cardoso, R.M.F.; Esteves da Silva, J.C.G. Advanced oxidation processes coupled with nanomaterials for water treatment. *Nanomaterials* **2021**, *11*, 2045. [CrossRef] [PubMed]
7. United States Environmental Protection Agency. *Handbook on Advanced Photochemical Oxidation Processes*; EPAl625/R-981004; United States Environmental Protection Agency: Washington, DC, USA, 1998.
8. Mierzwa, J.C.; Rodrigues, R.; Teixeira, A. UV-Hydrogen Peroxide Processes. In *Advanced Oxidation Processes for Wastewater Treatment: Emerging Green Chemical Technology*; Ameta, S.C., Ameta, R., Eds.; Academic Press: London, UK, 2018.
9. Silva, C.G.; Faria, J.L. Photochemical and photocatalytic degradation of an azo dye in aqueous solution by UV irradiation. *J. Photochem. Photobiol. A Chem.* **2003**, *155*, 133–143. [CrossRef]
10. Basturk, E.; Karatas, M. Decolorization of antraquinone dye Reactive Blue 181 solution by UV/H_2O_2 process. *J. Photochem. Photobiol. A Chem.* **2015**, *299*, 67–72. [CrossRef]
11. Tan, C.; Gao, N.; Zhou, S.; Xiao, Y.; Zhuang, Z. Kinetic study of acetaminophen degradation by UV-based advanced oxidation processes. *Chem. Eng. J.* **2014**, *253*, 229–236. [CrossRef]
12. Wang, Y.; Wang, Y.; Liu, Y. Absorption of H_2S from Gas Streams by the Wet Ultraviolet/Persulfate Oxidation Process: Mechanism and Kinetics. *Energy Fuels* **2020**, *34*, 8037–8045. [CrossRef]
13. Brienza, M.; Katsoyiannis, I.A. Sulfate Radical Technologies as Tertiary Treatment for the Removal of Emerging Contaminants from Wastewater. *Sustainability* **2017**, *9*, 1604. [CrossRef]
14. Baran, W.; Makowski, A.; Wardas, W. The effect of UV radiation absorption of cationic and anionic dye solutions on their photocatalytic degradation in the presence TiO_2. *Dyes Pigment.* **2008**, *76*, 226–230. [CrossRef]
15. Kasinathan, K.; Kennedy, J.; Elayaperumal, M.; Henini, M.; Malik, M. Photodegradation of organic pollutants RhB dye using UV simulated sunlight on ceria based TiO_2 nanomaterials for antibacterial applications. *Sci. Rep.* **2016**, *6*, 38064. [CrossRef]
16. Reza, K.; Kurny, A.; Gulshan, F. Parameters affecting the photocatalytic degradation of dyes using TiO_2: A review. *Appl. Water Sci.* **2017**, *7*, 1569–1578. [CrossRef]

17. Tlatelpa, T.; Trull, J.; Romeral, L. In situ Decolorization Monitoring of Textile Dyes for an Optimized UV-LED/TiO₂ Reactor. *Catalysts* **2019**, *9*, 669. [CrossRef]

18. El Mragui, A.; Zegaoui, O.; Esteves da Silva, J.C.G. Elucidation of the photocatalytic degradation mechanism of an azo dye under visible light in the presence of cobalt doped TiO₂ nanomaterials. *Chemosphere* **2021**, *266*, 128931. [CrossRef]

19. Liu, X.; Dai, L. Carbon-based metal-free catalysts. *Nat. Rev. Mater.* **2016**, *1*, 16064. [CrossRef]

20. Esteves da Silva, J.C.G.; Gonçalves, H.M.R. Analytical and bioanalytical applications of carbon dots. *Trends Anal. Chem.* **2011**, *30*, 1327–1336. [CrossRef]

21. Simões, E.; Leitão, J.; Esteves da Silva, J.C.G. Carbon dots from tryptophan doped glucose for peroxynitrite sensing. *Anal. Chim. Acta* **2014**, *852*, 174–180. [CrossRef] [PubMed]

22. Algarra, M.; Martin, M.P.; Rueda, M.C.; Jiménez-Jiménez, J.; Esteves da Silva, J.C.G.; Bandosz, T.; Castellón, E.R.; Casado, J.; López-Navarrete, J.T. Carbon Dots obtained using hydrothermal treatment of formaldehyde. Cell imaging in-vitro. *Nanoscale* **2014**, *6*, 9071–9077. [CrossRef]

23. Zhang, J.; Yu, S.-H. Carbon dots: Large-scale synthesis, sensing and bioimaging. *Mater. Today* **2016**, *19*, 382–393. [CrossRef]

24. Algarra, M.; Contreras-Caceres, R.; Bandosz, T.J.; Castellón, E.R.; Esteves da Silva, J.C.G.; Campos, B.B.; Jimenez-Jimenez, J. Carbon Dots as Fluorescent Sensor for Detection of Explosive Nitrocompounds. *Carbon* **2016**, *106*, 171–178. [CrossRef]

25. Chen, B.B.; Liu, M.L.; Li, C.M.; Huang, C.Z. Fluorescent carbon dots functionalization. *Adv. Colloid Interface Sci.* **2019**, *270*, 165–190. [CrossRef]

26. Sendão, R.M.S.; Crista, D.M.A.; Afonso, A.C.; de Yuso, M.M.; Algarra, M.; Esteves da Silva, J.C.G.; da Silva, L.P. Insight into the Hybrid Luminescence Showed by Carbon Dots and Molecular Fluorophores in Solution. *Phys. Chem. Chem. Phys.* **2019**, *21*, 20919–20926. [CrossRef]

27. Ge, G.; Li, L.; Wang, D.; Chen, M.; Zeng, Z.; Xiong, W.; Wu, X.; Guo, C. Carbon dots: Synthesis, properties and biomedical applications. *J. Mater. Chem. B* **2021**, *9*, 6553. [CrossRef]

28. Cui, L.; Ren, X.; Sun, M.; Liu, H.; Xia, L. Carbon Dots: Synthesis, Properties and Applications. *Nanomaterials* **2021**, *11*, 3419. [CrossRef]

29. Dager, A.; Uchida, T.; Maekawa, T.; Tachibana, M. Synthesis and characterization of Mono-disperse carbon Quantum Dots from fennel Seeds: Photoluminescence analysis using Machine Learning. *Sci. Rep.* **2019**, *9*, 14004. [CrossRef]

30. Huang, G.; Lin, Y.; Zhang, L.; Yan, Z.; Wang, Y.; Liu, Y. Synthesis of Sulfur-Selenium Doped Carbon Quantum Dots for Biological Imaging and Scavenging Reactive Oxygen Species. *Sci. Rep.* **2019**, *9*, 19651. [CrossRef] [PubMed]

31. Shen, S.; Li, R.; Wang, H.; Fu, J. Carbon Dot–Doped Titanium Dioxide Sheets for the Efficient Photocatalytic Performance of Refractory Pollutants. *Front. Chem.* **2021**, *9*, 706343. [CrossRef]

32. Atchudan, R.; Edison, T.; Perumal, S.; Vinodh, R.; Lee, Y. In-situ green synthesis of nitrogen-doped carbon dots for bioimaging and TiO₂ nanoparticles@nitrogen-doped carbon composite for photocatalytic degradation of organic pollutants. *J. Alloys Compd.* **2018**, *766*, 12–24. [CrossRef]

33. Ramachandran, P.; Lee, C.; Doong, R.; Oon, C.; Thanh, N.; Lee, H. A titanium dioxide/nitrogen-doped graphene quantum dot nanocomposite to mitigate cytotoxicity: Synthesis, characterisation, and cell viability evaluation. *RSC Adv.* **2020**, *10*, 21795. [CrossRef]

34. Jaiswal, A.; Ghosh, S.S.; Chattopadhyay, A. One step synthesis of C-dots by microwave mediated caramelization of poly(ethylene glycol). *Chem. Commun.* **2012**, *48*, 407–409. [CrossRef]

35. Peng, Z.; Ji, C.; Zhou, Y.; Zhao, T.; Leblanc, R.M. Polyethylene glycol (PEG) derived carbon dots: Preparation and applications. *Appl. Mat. Today* **2020**, *20*, 100677. [CrossRef]

36. Chen, S.; Jia, Q.; Zheng, X.; Wen, Y.; Liu, W.; Zhang, H.; Ge, J.; Wang, P. PEGylated carbon dot/MnO₂ nanohybrid: A new pH/H₂O₂-d-riven, turn-on cancer nanotheranostics. *Sci. China Mater.* **2018**, *61*, 1325–1338. [CrossRef]

37. Arsalania, N.; Nezhad-Mokhtaria, P.; Jabbari, E. Microwave-assisted and one-step synthesis of PEG passivated fluorescent carbon dots from gelatin as an efficient nanocarrier for methotrexate delivery. *Artif. Cells Nanomed. Biotechnol.* **2019**, *47*, 540–547. [CrossRef]

38. Yu, C.-H.; Wu, C.-H.; Ho, T.-H.; Hong, P.K.A. Decolorization of C.I. Reactive Black 5 in UV/TiO₂, UV/oxidant and UV/TiO₂/oxidant systems: A comparative study. *Chem. Eng. J.* **2010**, *158*, 578–583. [CrossRef]

39. Haji, S.; Benstaali, B.; Al-Bastaki, N. Degradation of methyl orange by UV/H₂O₂ advanced oxidation process. *Chem. Eng. J.* **2011**, *168*, 134–139. [CrossRef]

40. Feng, J.; Hu, X.; Po, L.Y. Discoloration and Mineralization of Orange II Using Different Heterogeneous Catalysts Containing Fe: A Comparative Study. *Environ. Sci. Technol.* **2004**, *38*, 5773–5778. [CrossRef] [PubMed]

41. El-Dein, A.; Libra, J.A.; Wiesmann, U. Mechanism and kinetic model for the decolorization of the azo dye Reactive Black 5 by hydrogen peroxide and UV radiation. *Chemosphere* **2003**, *52*, 1069–1077. [CrossRef]

42. Lucas, M.S.; Peres, J.A. Degradation of Reactive Black 5 by Fenton/UV-C and ferrioxalate/H₂O₂/solar light processes. *Dyes Pigment.* **2007**, *74*, 622–629. [CrossRef]

43. Hoang, N.T.; Nguyen, V.T.; Tuan, N.D.; Manh, T.D.; Le, P.-C.; Tac, D.; Mwazighe, F.M. Degradation of dyes by UV/Persulfate and comparison with other UV-based advanced oxidation processes: Kinetics and role of radicals. *Chemosphere* **2022**, *298*, 134197. [CrossRef]

44. Yu, X.; Sun, J.; Li, G.; Huang, Y.; Li, Y.; Xia, D.; Jiang, F. Integration of $SO_4{}^-$-based AOP mediated by reusable iron particles and a sulfidogenic process to degrade and detoxify Orange II. *Water Res.* **2020**, *174*, 115622. [CrossRef]

45. Fadaei, S.; Noorisepehr, M.; Pourzamani, H.; Salari, M.; Moradnia, M.; Darvishmotevalli, M.; Mengelizadeh, N. Heterogeneous activation of peroxymonosulfate with Fe_3O_4 magnetic nanoparticles for degradation of Reactive Black 5: Batch and column study. *J. Environ. Chem. Eng.* **2021**, *9*, 105414. [CrossRef]

46. Feng, S.; Xiao, B.; Wu, M.; Wang, Y.; Chen, R.; Liu, H. Copper phosphide: A dual-catalysis-center catalyst for the efficient activation of peroxydisulfate and degradation of Orange II. *Sep. Purif. Technol.* **2020**, *248*, 117004. [CrossRef]

47. Su, S.; Liu, Y.; He, W.; Tang, X.; Jin, W.; Zhao, Y. A novel graphene oxide-carbon nanotubes anchored α-FeOOH hybrid activated persulfate system for enhanced degradation of Orange II. *J. Environ. Sci.* **2019**, *83*, 73–84. [CrossRef]

48. Al-Mamun, M.; Hossain, K.T.; Mondal, S.; Khatun, M.; Islam, M.; Khan, D.M. Synthesis, characterization, and photocatalytic performance of methyl orange in aqueous TiO_2 suspension under UV and solar light irradiation. *S. Afr. J. Chem. Eng.* **2022**, *40*, 113–125. [CrossRef]

49. May-Lozano, M.; Lopez-Medina, R.; Escamilla, V.M.; Rivadeneyra-Romero, G.; Alonzo-Garcia, A.; Morales-Mora, M.; González-Díaz, M.O.; Martinez-Degadillo, S.A. Intensification of the Orange II and Black 5 degradation by sonophotocatalysis using Ag-graphene oxide/TiO_2 systems. *Chem. Eng. Process. Process Intensif.* **2020**, *158*, 108175. [CrossRef]

50. Sharma, S.K.; Bhunia, H.; Bajpai, P.K. Photocatalytic Decolorization Kinetics and Mineralization of Reactive Black 5 Aqueous Solution by UV/TiO_2 Nanoparticles. *CLEAN Soil Air Water* **2012**, *40*, 1290–1296. [CrossRef]

51. Szeto, W.; Li, J.; Huang, H.; Leung, D.Y.C. VUV/TiO_2 photocatalytic oxidation process of methyl orange and simultaneous utilization of the lamp-generated ozone. *Chem. Eng. Sci.* **2018**, *177*, 380–390. [CrossRef]

52. Marques, S.M.; Tavares, C.J.; Oliveira, L.F.; Oliveira-Campos, A.M.F. Photocatalytic degradation of C.I. Reactive Blue 19 with nitrogen-doped TiO_2 catalysts thin films under UV/visible light. *J. Mol. Struct.* **2010**, *983*, 147–152. [CrossRef]

53. Mokhtari, P.N.; Arsalani, N.; Ghorbani, M.; Hamishehkar, H. Development of biocompatible fluorescent gelatin nanocarriers for cell imaging and anticancer drug targeting. *J. Mater. Sci.* **2018**, *53*, 10679–10691. [CrossRef]

54. Mura, S.; Ludmerczki, R.; Stagi, L.; Garroni, S.; Carbonaro, C.M.; Ricci, P.C.; Casula, M.F.; Malfatti, L.; Innocenzi, P. Integrating sol-gel and carbon dots chemistry for the fabrication of fluorescent hybrid organic-inorganic films. *Sci. Rep.* **2020**, *10*, 4770. [CrossRef]

55. Ren, J.; Weber, F.; Weigert, F.; Wang, Y.; Choudhury, S.; Xiao, J.; Lauermann, I.; Genger, U.R.; Bande, A.; Petit, T. Influence of surface chemistry on optical, chemical and electronic properties of blue luminescent carbon dots. *Nanoscale* **2019**, *11*, 2056–2064. [CrossRef]

56. Gonzalez, J.D.; Arellano, J.C.; Luna, L.A.G.; Rojas, L.L. Photo-Fenton Degradation of RB5 Dye in Aqueous Solution Using Fe Supported on Mexican Natural Zeolite. *Int. J. Photoenergy* **2019**, *981631*. [CrossRef]

57. Chonga, M.N.; Tneua, Z.T.; Poha, P.E.; Arya, J.R. Synthesis, characterisation and application of TiO_2–zeolite nanocomposites for the advanced treatment of industrial dye wastewater. *J. Taiwan Inst. Chem. Eng.* **2015**, *50*, 288–296. [CrossRef]

58. Christé, S.; Esteves da Silva, J.C.G.; Pinto da Silva, L. Evaluation of the Environmental Impact and Efficiency of N-Doping Strategies in the Synthesis of Carbon Dots. *Materials* **2020**, *13*, 504. [CrossRef] [PubMed]

59. Crista, D.; Algarra, M.; Esteves da Silva, J.C.G.; Luque, R.; Pinto da Silva, L. Sustainable Production of Carbon Dots Nanoparticles from Spent Coffee Grounds. Sensing and Life Cycle Assessment Analysis. *Nanomaterials* **2020**, *10*, 1209. [CrossRef] [PubMed]

60. Crista, D.; Pinto da Silva, L.; Esteves da Silva, J.C.G. Evaluation of Different Bottom-up Routes for the Fabrication of Carbon Dots. *Nanomaterials* **2020**, *10*, 1316. [CrossRef] [PubMed]

61. Saha, D.; Desipio, M.M.; Hoinkis, T.J.; Smeltz, E.J.; Thorpe, R.; Hensley, D.K.; Fischer-Drowos, S.G.; Chen, J. Influence of hydrogen peroxide in enhancing photocatalytic activity of carbon nitride under visible light: An insight into reaction intermediates. *J. Environ. Chem. Eng.* **2018**, *6*, 4927–4936. [CrossRef]

62. Miller, C.M.; Valentine, R.L. Mechanistic Studies of Surface Catalysed H_2O_2 Decomposition and Contaminant Degradation in the Presence of Sand. *Water Res.* **1999**, *33*, 2805–2816. [CrossRef]